



HAL
open science

First super-pressure balloon-borne fine-vertical-scale profiles in the upper TTL: Impacts of atmospheric waves on cirrus clouds and the QBO

Martina Bramberger, M. Joan Alexander, Sean Davis, Aurelien Podglajen, Albert Hertzog, Lars Kalnajs, Terry Deshler, J. Douglas Goetz, Sergey Khaykin

► To cite this version:

Martina Bramberger, M. Joan Alexander, Sean Davis, Aurelien Podglajen, Albert Hertzog, et al.. First super-pressure balloon-borne fine-vertical-scale profiles in the upper TTL: Impacts of atmospheric waves on cirrus clouds and the QBO. *Geophysical Research Letters*, 2022, 49 (5), pp.e2021GL097596. 10.1029/2021GL097596 . insu-03594957

HAL Id: insu-03594957

<https://insu.hal.science/insu-03594957>

Submitted on 3 Mar 2022

HAL is a multi-disciplinary open access archive for the deposit and dissemination of scientific research documents, whether they are published or not. The documents may come from teaching and research institutions in France or abroad, or from public or private research centers.

L'archive ouverte pluridisciplinaire **HAL**, est destinée au dépôt et à la diffusion de documents scientifiques de niveau recherche, publiés ou non, émanant des établissements d'enseignement et de recherche français ou étrangers, des laboratoires publics ou privés.

1 First measurements of fine-vertical-scale wave impacts 2 on the tropical lower stratosphere

3 Martina Bramberger¹, M. Joan Alexander¹, Sean Davis², Aurelien Podglajen³,
4 Albert Hertzog³, Lars Kalnajs⁴, Terry Deshler⁴, J. Douglas Goetz⁴, Sergey
5 Khaykin⁵

6 ¹NorthWest Research Associates, Boulder Office, Colorado, USA

7 ²NOAA Chemical Sciences Laboratory, Boulder, CO, USA

8 ³Laboratoire de Météorologie Dynamique, Ecole Polytechnique, Palaiseau, France

9 ⁴Laboratory for Atmospheric and Space Physics, Boulder, CO, USA

10 ⁵Laboratoire Atmosphères, Observations Spatiales (LATMOS), UVSQ, Sorbonne Université, CNRS,
11 IPSL, Guyancourt, France

12 Key Points:

- 13 • Profiles from a long-duration balloon reveal equatorial waves with wide extent but
14 very fine-vertical scales.
- 15 • 97% of the cirrus clouds observed in the upper tropical tropopause layer (above
16 17 km) are related to these waves.
- 17 • The waves provide significant forcing to the QBO and could explain shortcomings
18 of models in simulating the QBO and its climate impacts.

Corresponding author: Martina Bramberger, martina@nwra.com

Abstract

Atmospheric waves in the tropical tropopause layer are recognized as a significant influence on processes that impact global climate. For example, waves drive the quasi-biennial oscillation (QBO) in equatorial stratospheric winds and modulate occurrences of cirrus clouds. However, the QBO in the lower stratosphere and thin cirrus have continued to elude accurate simulation in state-of-the-art climate models and seasonal forecast systems. We use first-of-their-kind profile measurements deployed beneath a long-duration balloon to provide new insights into impacts of fine-scale waves on equatorial cirrus clouds and the QBO just above the tropopause. Analysis of these balloon-borne measurements reveals previously uncharacterized fine-vertical-scale waves ($<1\text{km}$) with large horizontal extent ($>1000\text{km}$) and multiday periods. These waves affect cirrus clouds and QBO winds in ways that could explain current climate model shortcomings in representing these stratospheric influences on climate. Accurately simulating these fine-vertical-scale processes thus has the potential to improve sub-seasonal to near-term climate prediction.

Plain Language Summary

Instruments measuring temperature, water vapor, and ice particles were deployed on a 2-km-long string reeled up and down below a long-duration balloon drifting at 19 km in the lower stratosphere. The measurements reveal climate influences of very difficult-to-observe atmospheric waves with extreme aspect ratios: large horizontal scales ($>1000\text{km}$) but very short vertical scales ($<1\text{km}$). The waves are seen actively modifying properties of thin ice clouds that collectively influence tropical surface temperatures. An inverted Z-shape in the temperature profiles suggests these waves are intermittently breaking, like waves on a beach, leading to forces that drive zonal wind accelerations. The magnitude of these forces is strong, enough to drive the dominant zonal wind pattern called the Quasi-Biennial Oscillation (QBO), at least for the month-long period we observe. At these altitudes, the wave forces driving the QBO have been mysterious, despite worldwide efforts to simulate the QBO in climate models aiming to improve seasonal predictions.

1 Introduction

Tropical waves play a major role in driving large-scale atmospheric circulation (Baldwin et al., 2001) and generating cirrus clouds in the lower stratosphere (E. Jensen & Pfister, 2004; Schoeberl et al., 2015; Kim et al., 2016; Kärcher et al., 2019). These waves drive the quasi-biennial oscillation (QBO) in the zonal mean zonal wind in the lower stratosphere, and a growing body of evidence suggests that this oscillation is important to the intensity of the Madden-Julian oscillation (MJO) in tropical precipitation (Yoo & Son, 2016; Marshall et al., 2017; Lim et al., 2019) and climate prediction at seasonal to interannual time scales (Scaife et al., 2014; Smith et al., 2016; Garfinkel et al., 2018). By lowering the cold point temperature in the tropical tropopause layer (TTL), these waves also play a role in limiting the amount of water vapor in the stratosphere (Fueglistaler et al., 2009; Kim & Alexander, 2015). Stratospheric water vapor has an important greenhouse effect with radiative impacts comparable to other greenhouse gases that influence the global surface temperature (Forster & Shine, 2002; Solomon et al., 2010; Dessler et al., 2013; Banerjee et al., 2019), and also constitutes an important climate feedback. Therefore, for climate prediction it is vital to realistically simulate the QBO, TTL cirrus clouds and water vapor in the stratosphere, and all three still pose considerable challenges for current models.

Tropical waves comprise small-scale convective gravity waves (CGWs) and equatorial-trapped modes including large-scale inertia-gravity waves (IGWs), mixed Rossby-gravity waves, Kelvin waves and Rossby waves. These waves have periods ranging from minutes to weeks and zonal wavelengths spanning orders of magnitude from 1 km to 10000 km.

69 Particularly low-frequency IGW modes can pose a challenge for observations as their ver-
 70 tical wavelengths can become relatively very small, ≤ 1 km. Due to their fine vertical struc-
 71 ture these waves are unresolved in current global circulation models (GCMs) despite their
 72 long horizontal wavelengths.

73 Fine-vertical-scale waves have consequences for modeling TTL cirrus clouds (Boehm
 74 & Verlinde, 2000; E. Jensen & Pfister, 2004; Kim et al., 2016; E. J. Jensen et al., 2016)
 75 as they can cool air in the upper TTL thus lowering entry values of stratospheric wa-
 76 ter vapor (Kim & Alexander, 2015; Schoeberl et al., 2015). Large-horizontal-scale waves
 77 can develop very fine-vertical-scales in certain QBO shear conditions (Holton et al., 2001;
 78 Vincent & Alexander, 2020). Particularly at lower stratospheric altitudes, where mod-
 79 els most struggle to simulate realistic amplitude of the QBO (Bushell et al., 2020; Richter
 80 et al., 2020), unresolved fine-vertical-scale IGWs may be an important missing source
 81 of QBO forcing (Vincent & Alexander, 2020), and these lower stratospheric altitudes may
 82 be the most important region for simulating tropical stratospheric impacts on climate
 83 (Anstey et al., 2021).

84 Here, we use a unique data set collected during the Strateole-2 long-duration super-
 85 pressure balloon test campaign in 2019. During this campaign eight balloons were launched
 86 that circumnavigated Earth near the equator at flight altitudes ranging from 18 km to
 87 20 km (Haase et al., 2018; Corcos et al., 2021). We focus on balloon “TTL3” carrying
 88 a Thermodynamical SENSor (TSEN)(Hertzog et al., 2004) instrument and the Reel-down
 89 Aerosol Cloud Humidity and Temperature Sensor (RACHuTS)(Kalnajs et al., 2021). While
 90 the gondola TSEN measures temperature, pressure and horizontal wind at float level,
 91 RACHuTS provides high-resolution 2 km profiles of temperature, water vapor and aerosol
 92 at 1 m resolution below the balloon. We use these unique balloon measurements in con-
 93 junction with Constellation Observing System for Meteorology, Ionosphere, and Climate-
 94 2 (COSMIC-2) satellite observations and the fifth generation European Centre for Medium-
 95 Range Weather Forecasts (ECMWF) atmospheric reanalysis (ERA5), to provide for the
 96 first time, a classification of long-period waves with short vertical wavelengths and an
 97 assessment of their impact on cirrus clouds and the QBO in the lowermost tropical strato-
 98 sphere.

99 1.1 Instruments and Datasets

100 The flight-level TSEN provides ambient air temperature and pressure measurements
 101 and GPS position at the isopycnic level of the drifting Strateole 2 balloon gondola. The
 102 TSEN data are available every 30 s. The temperature sensor accuracy is 0.1 K at night
 103 and 0.25 K during the day after correction for solar radiation (Hertzog et al., 2004). The
 104 absolute accuracy and precision of the pressure sensor are ± 2 hPa and 0.01 hPa. Winds
 105 are derived from position with 0.1 ms^{-1} precision.

106 RACHuTS is a system designed to measure profiles down to 2 km below the flight
 107 level of a super pressure balloon(Kalnajs et al., 2021). It lowers and retracts an instru-
 108 ment package consisting of a TSEN temperature sensor, a water vapor sensor, and an
 109 aerosol spectrometer. The TSEN temperature sensor is a simplified version of the sen-
 110 sor described above. The water vapor sensor is a Fluorescence Lyman-Alpha Stratospheric
 111 Hygrometer (FLASH-B) and reports water vapor at 1 Hz with a precision of 5-6% in the
 112 stratosphere, where the accuracy is limited by the calibration error of 4%. RACHuTS
 113 data are only collected at night where the solar zenith angle is $>95^\circ$ to ensure optimal
 114 sampling conditions for FLASH-B. The RACHuTS Optical Particle Counter uses Mie
 115 theory and side-scattered light by particles, from the laser illuminated sample stream,
 116 to measure the concentrations of the particles in eight size bins between $0.3\text{-}10 \mu\text{m}$ di-
 117 ameter. The concentrations of smallest particles, diameter $>0.3 \mu\text{m}$, are measured at 1 Hz,
 118 larger particles ($0.5 - 10 \mu\text{m}$) have an 8 s integration time. The upper size limit of the

119 instrument is indefinite, all that can be determined is that a particle is larger than 10 μm .
 120 The sample flow rate is 3.5 liters per minute.

121 Here we use the aerosol counter to identify the presence of ice particles. This is done
 122 using a size threshold of 3 μm . There are no instruments which can unambiguously iden-
 123 tify ice at such small sizes, but as with numerous other studies we infer the presence of
 124 ice from measurements of particles with a size which is unlikely to appear at that alti-
 125 tude as a dry particle (Thomas et al., 2002; Krämer et al., 2009; Davis et al., 2010). For
 126 the RACHuTS profiles there are many observations of the size distribution of aerosol larger
 127 than 0.3 μm , and nearly all instances of the presence of particles larger than 3, 5, and
 128 10 μm are associated with conditions favorable for the existence of ice.

129 COSMIC-2 was launched in June 2019 and is a successor of the COSMIC mission
 130 launched in 2006 (Schreiner et al., 2020). It consists of 6 satellites orbiting Earth on a
 131 low geocentric orbit, that carry advanced Tri-GNSS (Global Navigation Satellite Sys-
 132 tem) Radio Occultation receivers. We use COSMIC-2 dry temperature profiles that are
 133 valid from the upper troposphere up to 40 km provided at vertical resolution ~ 100 m with
 134 accuracy < 0.1 K.

135 ERA5 is an atmospheric reanalysis provided by ECMWF (Hersbach et al., 2020).
 136 ERA5 data are available at 6 hour intervals on 137 levels up to 1 Pa with a horizontal
 137 resolution of 31 km. The distance between the different vertical levels is about 400 m in
 138 the lower stratosphere. We note that ERA5 might show significant errors in the equa-
 139 torial lower stratosphere which is a challenging region for reanalyses (Podglajen et al.,
 140 2014)

141 2 Methods

142 2.1 Wave temperature perturbations in RACHuTS profiles

143 For the calculation of wave temperature perturbations we use COSMIC-2 obser-
 144 vations to derive background temperature profiles. A background profile is defined as
 145 an average in a box that is $5^\circ \times 10^\circ$ latitude \times longitude and 30 days in time. The box
 146 moves with the balloon along its flight track. The temperature perturbations from RACHuTS
 147 observations are calculated by subtracting the COSMIC-2 background temperature pro-
 148 file at the location and time of a RACHuTS profile. The perturbations so defined include
 149 waves with periods < 30 days (Kim et al., 2016).

150 An adiabatic temperature profile gradient can be evidence for vertical mixing. Note
 151 that for temperature perturbations, the vertical gradient corresponding to an adiabtic
 152 lapse rate depends on the background temperature gradient $d\bar{T}/dz$ and can be written:

$$\left(\frac{dT'}{dz}\right)_{ad} = -\frac{g}{c_p} - \frac{d\bar{T}}{dz} \quad (1)$$

153 where g is the gravitational acceleration, c_p is the specific heat at constant pressure, $(dT'/dz)_{ad}$
 154 is the temperature perturbation gradient that would make the total lapse rate adiabatic.
 155 Eq.1 is derived assuming that the total temperature lapse rate $-(dT/dz)_{ad}$ equals the
 156 adiabatic lapse rate such that,

$$\left(\frac{dT}{dz}\right)_{ad} = \frac{d\bar{T}}{dz} + \left(\frac{dT'}{dz}\right)_{ad} = -\frac{g}{c_p}. \quad (2)$$

157 $d\bar{T}/dz$ is derived from COSMIC2 background temperature profiles between 17km and
 158 19km altitude where RACHuTS profiles are available.

159 Wave vertical wavelengths will be key to identifying the type of wave. Due to the
 160 RACHuTS profile length only waves with vertical wavelengths smaller than 2 km are fully

161 resolved. Using a S-transform (Stockwell et al., 1996) spectral analysis we derive the ver-
 162 tical wavelengths from the RACHuTS profiles.

163 2.2 Calculation of total wave energy

164 Because the super-pressure balloons drift with the ambient wind, analysis of the
 165 wind and temperature perturbations in the TSEN observations permit direct estimates
 166 of wave intrinsic periods. The perturbations from TSEN observations are calculated by
 167 subtracting a 30 day running mean value of the respective quantity. We decompose the
 168 total perturbation energy (E_{tot}) from the in situ observed wind and temperature per-
 169 turbations along the flight track into time and frequency spectrum using the S-transform
 170 (Stockwell et al., 1996). The total energy spectrum is given by

$$E_{tot} = 0.5 \left[(\hat{u}^2 + \hat{v}^2) + \frac{g^2}{N^2} \frac{\hat{T}^2}{\bar{T}} \right]. \quad (3)$$

171 N is the static stability, g the gravitational acceleration, \bar{T} is the background temper-
 172 ature, \hat{u} and \hat{v} are the zonal and meridional wind amplitudes, and \hat{T} the temperature
 173 amplitude.

174 2.3 Wave Momentum Flux and Drag calculation

175 The drag force exerted on the atmosphere from IGWs is calculated as the diver-
 176 gence of momentum flux, or

$$F_{local} = -\frac{1}{\rho} \frac{d(\overline{\rho u'w'})}{dz} \quad (4)$$

177 with the density ρ and the zonal momentum flux ($\overline{\rho u'w'}$). Following (Sato & Dunker-
 178 ton, 1997), $\overline{u'w'}$ associated with IGWs in QBO shear conditions is given by,

$$\overline{u'w'} = \frac{2g\omega}{N\bar{T}} \left(\frac{\delta u}{\delta z} \right)^{-1} \overline{u'T'} \quad (5)$$

179 where g is the gravitational acceleration, ω the intrinsic frequency, N the static stabil-
 180 ity, \bar{T} the mean temperature, $\frac{\delta u}{\delta z}$ the vertical shear of zonal background wind and $\overline{u'T'}$
 181 the zonal heatflux calculated as cospectrum of zonal wind and temperature perturba-
 182 tions. The parameters N and \bar{T} are derived from COSMIC 2 observations, and $\frac{\delta u}{\delta z}$ from
 183 ERA5, while ω and $\overline{u'T'}$ are calculated from TSEN measurements. That way our mo-
 184 mentum flux estimate is primarily based on observations.

185 We assume the wave momentum flux will dissipate between the balloon observa-
 186 tion level and the wave critical level.

187 Since the IGWs discussed in this study have limited zonal extent while QBO forc-
 188 ing is a zonal-mean concept, we estimate the zonal-mean drag of the IGWs by apply-
 189 ing an area factor A to the local drag F_{local}

$$\bar{F}_{zonal} = F_{local} \times A \quad (6)$$

190 where overbars denote zonal means. Here, following we assume A to be proportional three
 191 times the zonal wavelength of the observed IGWs divided by Earth's circumference (Vincent
 192 & Alexander, 2020).

193 3 Results

194 We focus on the time period from 9th December 2019 to 9th January 2020 where
 195 the TTL3 balloon drifted in eastward QBO winds at 66hPa from the Pacific across South
 196 America to the Atlantic ocean towards Africa (Fig.1). This time period includes 30 RACHuTS
 197 profiles between 27 Dec – 5 Jan (4.5°N/172.4°W – 0.5°N/15.5°W).

198

3.1 RACHuTS observed Wave Amplitudes

199

200

201

202

203

The temperature perturbation (T') profiles derived from RACHuTS observations show signatures of large amplitude waves and evidence of turbulent mixing layers due to convective instability (see Fig.1). The measurements are primarily above the mean tropopause (defined by COSMIC-2 balloon-following background), which occurs at 17.2 ± 0.3 km with a temperature of 191 ± 3 K.

204

205

206

207

208

209

210

211

Many of the profiles exhibit a distinct inverted Z-shape with shallow positive vertical T' gradients above and below layers with near-adiabatic lapse rate of varying depths (e.g. 31st December 2019 with a depth of about 600 m). As also shown in (Podglajen et al., 2017), the near-adiabatic layers are related to the less stable $dT'/dz < 0$ phase of low frequency waves, and these layers are likely remnants of convective instability and turbulent mixing in the unstable phase of these waves. Unlike (Podglajen et al., 2017), our data permit analysis of wave type, frequency, and horizontal scale (sec. 3.3), which suggest these mixed layers have wide horizontal extent.

212

3.2 Ice Clouds and Wave Interactions

213

214

215

216

217

218

219

220

The RACHuTS ice particle detections, defined by particle sizes $> 3 \mu\text{m}$, are highlighted with black dots in Fig.1. The particle concentration in these regions is on the order of 3/liter. On two occasions concentrations exceeded 6/liter and in 20% of the cases $5 \mu\text{m}$ particles were also observed. Thus these are very thin clouds, invisible to remote sensors, and the ice particles grow slowly with a limited vapor supply. In several of the clouds, the concentration of $2 \mu\text{m}$ particles was increased to 6-15/liter, well above the bulk of aerosol concentrations at this size, indicating that these particles were probably also ice.

221

222

223

224

225

226

227

228

229

Previous studies have shown that ice cloud occurrences in the TTL are related to wave temperature changes (Kim et al., 2016; Chang & L'Ecuyer, 2020). The influence of waves on clouds is primarily determined by the cold ($T' < 0$) or warm ($T' > 0$) phase of the wave, but also by the wave-induced cooling rate, which is proportional to the change in phase with height dT'/dz (Kim et al., 2016; Podglajen et al., 2018). Following previous studies we evaluate ice cloud detections as a function of the four phases corresponding to positive or negative wave perturbations (T') and their vertical gradients dT'/dz proportional to cooling rate (Kim et al., 2016; Chang & L'Ecuyer, 2020), and as a function of ice relative humidity (Fig.2).

230

231

232

233

234

235

236

237

In concurrence with previous studies (Kim et al., 2016; Chang & L'Ecuyer, 2020) our analysis shows that 90% of sub visible cirrus cloud detections at upper TTL altitudes, above the mean cold point, occur in the cold phase of waves (left half of Fig.2). Most of the detections (67%) are in the cold phase of the wave while it is also actively cooling. Colors in Fig.2 show more extreme supersaturation occurs at larger negative wave perturbations, and supersaturation is rather less sensitive to the cooling rates. The strong relationships between ice cloud occurrence, extreme supersaturations, and waves raise the question, what types of waves are generating these sub visible clouds?

238

3.3 Wave Type Identification

239

240

241

242

Identifying the wave types will permit estimation of their horizontal scales and their effects on the QBO winds. In the time period of interest the balloon drifted in westerly QBO winds (Fig. 3a). The wave energy spectrum per unit density E_{tot} (Fig.4, Eq.(3)) exhibits enhanced values at intrinsic periods of 2.5 – 5 days, and 11.5 – 15 days.

243

244

245

To provide further insight into the regions of enhanced E_{tot} (3), we use the RACHuTS vertical temperature perturbation profiles (Fig.1). We use the example of the 29th December 2019 to explain the analysis. The vertical wavelength derived from the observa-

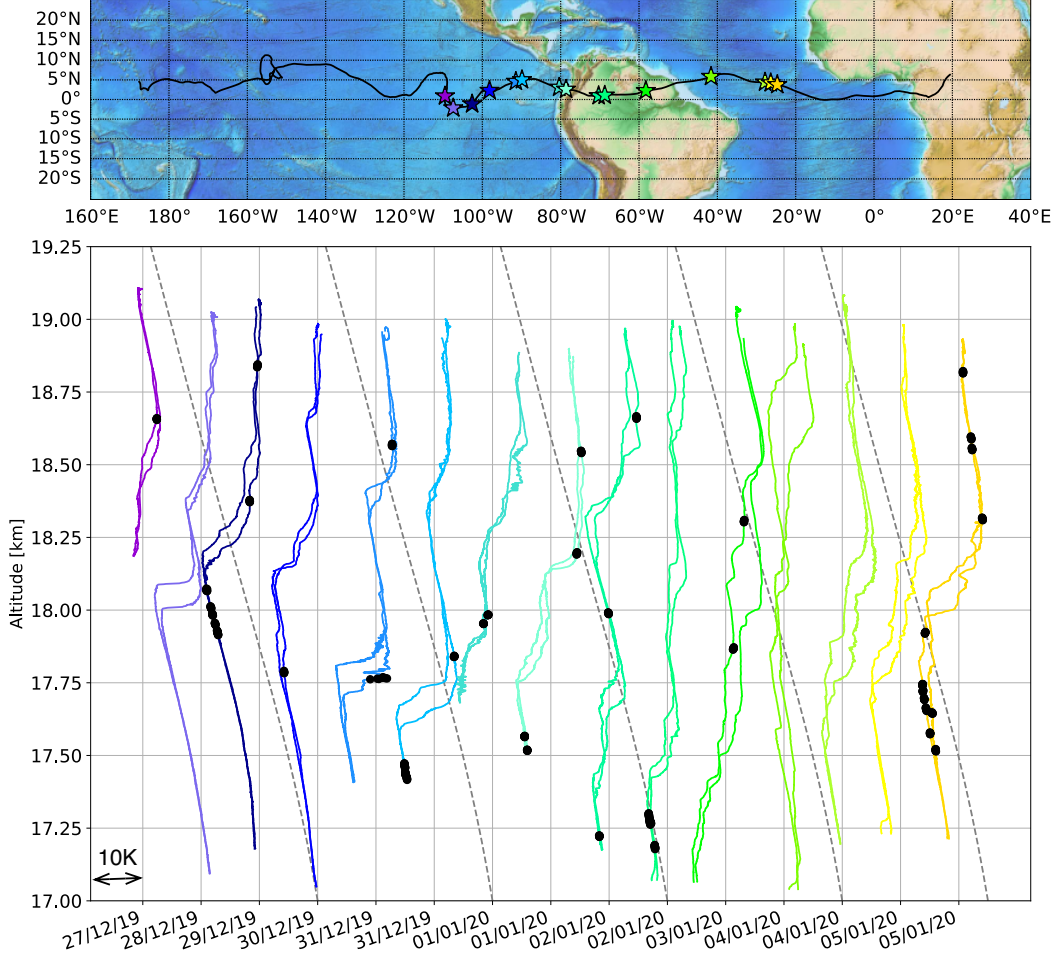


Figure 1. Flight track of the TTL3 balloon during the Strateole-2 campaign from 9th December to 9th January. The stars show the positions of the pairs of descending/ascending RACHuTS temperature perturbation profiles shown in the lower panel. Each pair of RACHuTS profiles are separated by 10K. The color coding corresponds to the location of the profile (see map) and the date of the profile pair is given on the x-axis. The gray vertical lines highlight $T' = 0$ for each night's pair of profiles. Temperature perturbations are due to waves with periods < 30 days. Black dots represent the location of ice observations and the black dashed lines show the slope of perturbations giving a net adiabatic lapse rate, indicating mixed layers.

246 tion on 29th December is 875 m. Assuming that the vertical RACHuTS profiles sample
 247 the waves observed with the in-situ TSEN measurements we use the dispersion relation-
 248 ships (Andrews et al., 1987) with the observed vertical wavelengths and the TSEN ob-
 249 served intrinsic periods to attribute the peaks in the total energy spectrum to specific
 250 wave types. Specifically, the peak at intrinsic period of 4.8 days on 29th December is iden-
 251 tified as an $n=0$ eastward propagating IGW (EIGW) with zonal wavenumber 18 (WN18)
 252 (Kiladis et al., 2009). Considering all available RACHuTS profiles that are at least 1200 m
 253 long (i.e. all profiles except 28th December and 1st January) we attribute the enhanced
 254 total energies to a $n=0$ EIGW packet with wavenumbers ranging from ~ 18 to 27 ($\lambda_h =$
 255 2666 km – 1481 km) for the intrinsic period of 4.8 days and $n=1$ WN23 and 31 EIGWs

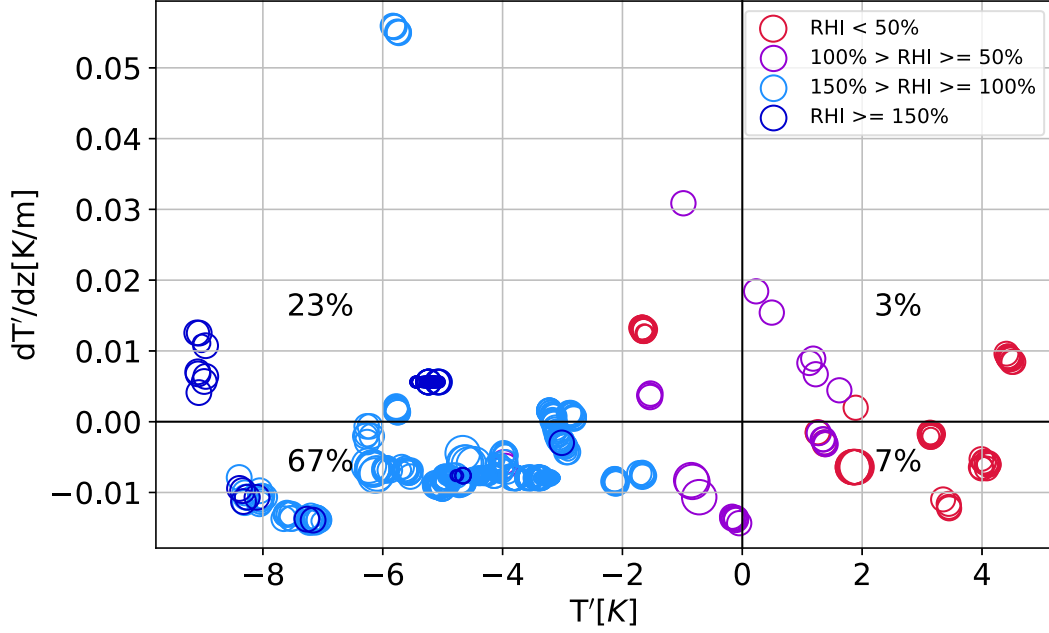


Figure 2. Wave influence on cirrus cloud detections at and around South America. The plot shows the distribution of particles $\geq 3\mu\text{m}$, considered to be ice, as a function of wave perturbations (T') and the vertical gradient of the temperature perturbation T' ($dT'/dz \sim dT'/dt$). The colors refer to relative humidity above ice (RHI) and the percentages given in the quadrants are the percentage of particles found in the respective quadrant relative to all particle counts. The circle sizes are proportional to particle concentrations where small circles represent 1/liter, medium size circles 3/liter and the largest circles 6/liter.

256 ($\lambda_h = 1739 \text{ km} - 1290 \text{ km}$) for an intrinsic period of 3.5 days. The intrinsic phase speed
 257 of both wave packets is $\sim 5 \text{ ms}^{-1}$.

258 So far we could attribute the enhanced total energy levels to specific wave types
 259 only for times where RACHuTS observations are available. To identify wave types out-
 260 side the period covered with RACHuTS observations we need supplemental information
 261 from ERA5 analyses. Both, the observation (Fig.4 a) and the ERA5 analyses (Fig.4 b)
 262 exhibit elevated levels of total energy at periods 11.5–15 days from 9th December to 27th
 263 December (black box in Fig. 4). These energies are consistent with a $n = 1$ Rossby wave
 264 with a long vertical structure that is resolved in ERA5 reanalyses (Fig.4 b). On the con-
 265 trary EIGW energy at 2.5–5 days is strongly underestimated in ERA5, likely due to its
 266 too coarse vertical resolution.

267 To understand the elevated energy levels with intrinsic periods between 2.5 and 5 days
 268 outside the time-period of RACHuTS observations we calculate the Doppler-shift of wave
 269 intrinsic periods along the TTL3 flight track. For this analysis we use ERA5 zonal wind,
 270 smoothed over 8 days as background winds (Fig. 3b) and linear wave theory (Andrews
 271 et al., 1987). The gray dashed lines in Fig.4a show the backward and forward evolution
 272 of intrinsic periods for the EIGW packets previously identified, based on the ERA5 back-
 273 ground wind (Fig.3b). The colored dots highlight the respective starting dates and in-
 274 trinsic periods. The Doppler shifted intrinsic periods starting between 29th December
 275 and 2nd January align well with the evolution of the total energy peak between 17th De-
 276 cember and about 2nd January. Therefore, we associate shifts in enhanced energies with
 277 intrinsic periods from about 3.5 days to 5 days in that time frame to Doppler shifted EIGWs

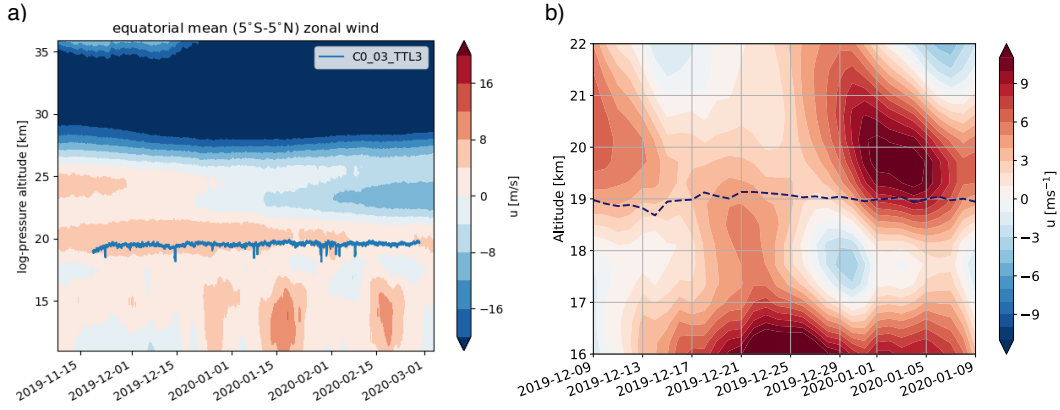


Figure 3. Equatorial zonal winds simulated by ERA5. a) Time-height variations in zonal mean zonal wind averaged between 5°SN and 5°S with the balloon altitude (blue line). The zonal mean zonal wind shows the structure of the QBO above the tropopause. b) Eight-day-running-mean zonal wind along the balloon flight-track as a function of altitude and time. The dark-blue dashed line shows the daily averaged altitude of the balloon.

278 with WN18–27. The Doppler shifted intrinsic periods starting on 4th and 5th of Jan-
 279 uary connect well the enhanced total energies from 13th December to 5th January. As
 280 the intrinsic periods on 13th December are consistent with the wave properties observed
 281 between 5th and 9th January, we hypothesize that the elevated total energies on the 13th
 282 December 2019 are of similar wave type as observed on 4th and 5th January. This anal-
 283 ysis highlights the widespread occurrence of EIGWs for intrinsic periods between 2.5 and
 284 5 days.

285 We estimate the zonal mean force of the observed EIGWs $\sim 0.5 \text{ ms}^{-1} \text{ day}^{-1}$ which
 286 is close to the magnitude of the total wave forcing necessary to drive the QBO in mod-
 287 els at these levels (Holt et al., 2016, 2020; Pahlavan et al., 2021). Considering the ap-
 288 proximate ground-based phase speed of 12 ms^{-1} and the background zonal wind profile
 289 (Fig. 3b) this forcing estimate is based on the assumption that the waves will encounter
 290 a critical level ($c=u$) within 1 km above the balloon flight track (see Fig. 3b) and dissi-
 291 pate completely. The forcing is valid at $\sim 19\text{--}20$ km, which is near the bottom of the QBO,
 292 an important region where the QBO may impact surface climate and where most GCMs
 293 underestimate the variability in the QBO winds (Bushell et al., 2020).

294 4 Summary and Discussions

295 The measurements presented allow for the first time to identify large-scale waves
 296 with fine vertical scales as equatorial EIGWs in the upper TTL/lowermost stratosphere,
 297 and to determine their impact on cirrus clouds and QBO forcing.

298 4.1 Significance to Ice Clouds Modeling

299 Our analysis shows that 97% of the ice clouds observed were related to EIGW ac-
 300 tivity (see Fig.2). These cirrus clouds are extremely thin and subvisible to satellite ob-
 301 servations. Previous observations have identified Kelvin wave influences on cirrus in the
 302 TTL (Boehm & Verlinde, 2000; Holton et al., 2001; Fujiwara et al., 2009), and theoret-
 303 ical studies stress the importance of high-frequency waves in the generation of cirrus clouds
 304 (E. Jensen & Pfister, 2004; Kärcher et al., 2019). The present observations add to these
 305 mechanisms the modulation of thin cirrus clouds by equatorial IGW with long horizon-

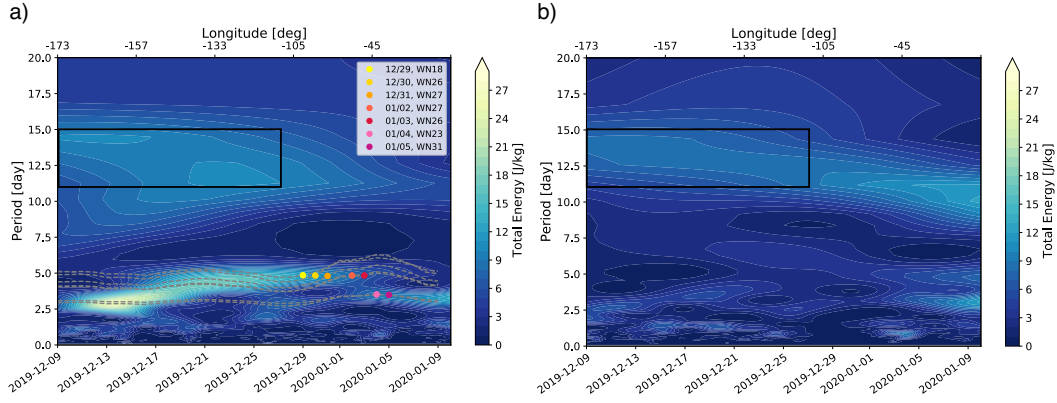


Figure 4. Wave energy spectrum E_{tot} (color shading) as a function of time and wave period from the balloon flight-level TSEN observations (a) and ERA5 (b). The color bar refers to E_{tot} and the gray dashed lines show the theoretical intrinsic period variations in time for eastward inertia gravity waves with zonal wavenumbers ranging from 15 to 28. The colored points in (a) highlight the starting points based on RACHuTS observed wavelengths from which the intrinsic periods have been calculated backwards and forwards in time. Periods and dates suggestive of Rossby waves are highlighted with a black box.

306 tal wavelengths (1000s of km) and short vertical wavelengths (< 1 km). Including these
 307 equatorial IGWs may help explain the widespread occurrence of thin cirrus layers in the
 308 upper TTL.

309 The finding that the cold phase of these EIGWs generates ice suggests that they
 310 could be impacting the entry value of stratospheric water vapor through additional de-
 311 hydration events as air ascends into the stratosphere if the environment remains super-
 312 saturated long enough to grow the ice crystals to sizes large enough to sediment out. In
 313 particular, the fact that the EIGW-generated clouds occur near and above the clima-
 314 tological cold point tropopause (~ 380 K) with periods of 2–5 days means that they could
 315 be dehydrating air masses that would otherwise not undergo further dehydration (all RACHuTS-
 316 measured clouds occurred above 373K). However, it is impossible with the present study
 317 to quantify potential contribution of EIGWs to stratospheric water vapor, and additional
 318 measurements are needed to quantify whether this contribution is significant.

319 4.2 Implications for Simulating the QBO

320 The EIGWs detected herein are characterized by very long horizontal scales, but
 321 very short vertical scales at and below the vertical resolution of modern GCMs and satel-
 322 lite observations. Our estimate of the contribution of the EIGWs to the forcing of the
 323 QBO is substantial as it is comparable to the total forcing of the QBO at lowermost strato-
 324 sphere levels (Holt et al., 2016). At the observed EIGW breaking altitudes, GCMs con-
 325 sistenty underestimate the amplitude of the QBO (Bushell et al., 2020). Comparison of
 326 total energy spectra from flight-level TSEN observations and ERA5 shows that these types
 327 of waves are missing even in state-of-the-art reanalyses (Fig.4). Therefore, the models
 328 also miss the forcing exerted by short-vertical wavelength IGWs in the lowermost strato-
 329 sphere, and these waves might be key for the realistic simulation of the QBO and its in-
 330 teraction with the MJO in the lowermost stratosphere.

Acknowledgments

We thank Robert Vincent for helpful discussions about waves in superpressure balloon data. The TSEN and RACHuTS data were collected as part of Strateole-2, which is sponsored by CNES, CNRS/INSU and NSF. Joan Alexander and Martina Bramberger were supported by NSF grants 1642246 and 1642644. The RACHuTS measurements were completed under support from NSF award 1643022. Strateole-2 data is available on <https://data.ipsl.fr/catalog/strateole2/> including RACHuTS data. COSMIC-2 data was downloaded from <https://cdaac-www.cosmic.ucar.edu> and ERA5 is available on <https://www.ecmwf.int/en/forecasts/dataset/ecmwf-reanalysis-v5>.

References

- Andrews, D. G., Holton, J. R., & Leovy, C. B. (1987). *Middle atmosphere dynamics*.
- Anstey, J. A., Simpson, I. R., Richter, J. H., Naoe, H., Taguchi, M., Serva, F., . . . Yukimoto, S. (2021). Teleconnections of the quasi-biennial oscillation in a multi-model ensemble of QBO-resolving models. *Quart. J. Roy. Meteor. Soc.*, 1–25. doi: 10.1002/qj.4048
- Baldwin, M. P., Gray, L. J., Dunkerton, T. J., Hamilton, K., Haynes, P. H., Randel, W. J., . . . Takahashi, M. (2001). The quasi-biennial oscillation. *Rev. Geophys.*, 39(2), 179–229. doi: <https://doi.org/10.1029/1999RG000073>
- Banerjee, A., Chiodo, G., Previdi, M., Ponater, M., Conley, A., & Polvani, L. (2019, 08). Stratospheric water vapor: an important climate feedback. *Climate Dynamics*. doi: 10.1007/s00382-019-04721-4
- Boehm, M. T., & Verlinde, J. (2000). Stratospheric influence on upper tropospheric tropical cirrus. *Geophys. Res. Lett.*, 27(19), 3209–3212. doi: <https://doi.org/10.1029/2000GL011678>
- Bushell, A. C., Anstey, J. A., Butchart, N., Kawatani, Y., Osprey, S. M., Richter, J. H., . . . Yukimoto, S. (2020). Evaluation of the Quasi-Biennial Oscillation in global climate models for the SPARC QBO-initiative. *Quart. J. Roy. Meteor. Soc.* doi: 10.1002/qj.3765
- Chang, K.-W., & L’Ecuyer, T. (2020). Influence of gravity wave temperature anomalies and their vertical gradients on cirrus clouds in the tropical tropopause layer – a satellite-based view. *Atmos. Chem. and Phys.*, 20(21), 12499–12514. doi: 10.5194/acp-20-12499-2020
- Corcos, M., Hertzog, A., Plougonven, R., & Podglajen, A. (2021). Observation of Gravity Waves at the Tropical Tropopause Using Superpressure Balloons. *J. Geophys. Res. Atmos.*, 126(15), e2021JD035165. doi: <https://doi.org/10.1029/2021JD035165>
- Davis, S., Hlavka, D., Jensen, E., Rosenlof, K., Yang, Q., Schmidt, S., . . . Bui, T. P. (2010). In situ and lidar observations of tropopause subvisible cirrus clouds during TC4. *J. Geophys. Res. Atmos.*, 115(D10). doi: <https://doi.org/10.1029/2009JD013093>
- Dessler, A. E., Schoeberl, M. R., Wang, T., Davis, S. M., & Rosenlof, K. H. (2013). Stratospheric water vapor feedback. *Proceedings of the National Academy of Sciences*. doi: 10.1073/pnas.1310344110
- Forster, P. M. d. F., & Shine, K. P. (2002). Assessing the climate impact of trends in stratospheric water vapor. *Geophys. Res. Lett.*, 29(6), 10-1-10-4. doi: <https://doi.org/10.1029/2001GL013909>
- Fueglistaler, S., Dessler, A. E., Dunkerton, T. J., Folkins, I., Fu, Q., & Mote, P. W. (2009). Tropical tropopause layer. *Reviews of Geophysics*, 47(1). doi: <https://doi.org/10.1029/2008RG000267>
- Fujiwara, M., Iwasaki, S., Shimizu, A., Inai, Y., Shiotani, M., Hasebe, F., . . . Yoneyama, K. (2009). Cirrus observations in the tropical tropopause layer over the western Pacific. *J. Geophys. Res. Atmos.*, 114(D9). doi:

- 384 <https://doi.org/10.1029/2008JD011040>
- 385 Garfinkel, C. I., Schwartz, C., Domeisen, D. I. V., Son, S.-W., Butler, A. H., &
386 White, I. P. (2018). Extratropical atmospheric predictability from the quasi-
387 biennial oscillation in subseasonal forecast models. *J. Geophys. Res.: Atmos.*,
388 *123*(15), 7855-7866. doi: 10.1029/2018JD028724
- 389 Haase, J., Alexander, M., Hertzog, A., Kalnajs, L., Deshler, T., Davis, S., ... Venel,
390 S. (2018). Around the world in 84 days. *EOS*, 99. doi: [https://doi.org/](https://doi.org/10.1029/2018EO091907)
391 [10.1029/2018EO091907](https://doi.org/10.1029/2018EO091907)
- 392 Hersbach, H., Bell, B., Berrisford, P., Hirahara, S., Horányi, A., Muñoz Sabater,
393 J., ... Thópaút, J.-N. (2020). The ERA5 global reanalysis. *Quart. J. Roy.
394 Meteor. Soc.*, *146*(730), 1999-2049. doi: <https://doi.org/10.1002/qj.3803>
- 395 Hertzog, A., Basdevant, C., Vial, F., & Mechoso, C. R. (2004). The accuracy
396 of stratospheric analyses in the northern hemisphere inferred from long-
397 duration balloon flights. *Q.J.R. Meteorol. Soc.*, *130*(597), 607-626. doi:
398 <https://doi.org/10.1256/qj.03.76>
- 399 Holt, L. A., Alexander, M. J., Coy, L., Molod, A., Putman, W., & Pawson,
400 S. (2016). Tropical Waves and the Quasi-Biennial Oscillation in a 7-
401 km Global Climate Simulation. *J. Atmos. Sci.*, *73*(9), 3771-3783. doi:
402 [10.1175/JAS-D-15-0350.1](https://doi.org/10.1175/JAS-D-15-0350.1)
- 403 Holt, L. A., Lott, F., Garcia, R. R., Kiladis, G. N., Cheng, Y.-M., Anstey, J. A.,
404 ... Yukimoto, S. (2020). An evaluation of tropical waves and wave forc-
405 ing of the QBO in the QBOi models. *Q J R Meteorol Soc.*, *n/a*(n/a). doi:
406 <https://doi.org/10.1002/qj.3827>
- 407 Holton, J. R., Alexander, M. J., & Boehm, M. T. (2001). Evidence for short vertical
408 wavelength Kelvin waves in the Department of Energy-Atmospheric Radiation
409 Measurement Nauru99 radiosonde data. *J. Geophys. Res. Atmos.*, *106*(D17),
410 20125-20129. doi: <https://doi.org/10.1029/2001JD900108>
- 411 Jensen, E., & Pfister, L. (2004). Transport and freeze-drying in the tropical
412 tropopause layer. *J Geophys Res Atmos*, *109*(D2). doi: [https://doi.org/](https://doi.org/10.1029/2003JD004022)
413 [10.1029/2003JD004022](https://doi.org/10.1029/2003JD004022)
- 414 Jensen, E. J., Ueyama, R., Pfister, L., Bui, T. V., Alexander, M. J., Podglajen, A.,
415 ... Schoeberl, M. R. (2016). High-frequency gravity waves and homogeneous
416 ice nucleation in tropical tropopause layer cirrus. *Geophys Res Lett*, *43*(12),
417 6629-6635. doi: <https://doi.org/10.1002/2016GL069426>
- 418 Kalnajs, L. E., Davis, S. M., Goetz, J. D., Deshler, T., Khaykin, S., St. Clair, A.,
419 ... Lykov, A. (2021). A reel-down instrument system for profile measure-
420 ments of water vapor, temperature, clouds, and aerosol beneath constant-
421 altitude scientific balloons. *Atmos. Meas. Tech.*, *14*(4), 2635-2648. doi:
422 [10.5194/amt-14-2635-2021](https://doi.org/10.5194/amt-14-2635-2021)
- 423 Kärcher, B., Jensen, E. J., & Lohmann, U. (2019). The Impact of Mesoscale Grav-
424 ity Waves on Homogeneous Ice Nucleation in Cirrus Clouds. *Geophys Res Lett*,
425 *46*(10), 5556-5565. doi: <https://doi.org/10.1029/2019GL082437>
- 426 Kiladis, G. N., Wheeler, M. C., Haertel, P. T., Straub, K. H., & Roundy, P. E.
427 (2009). Convectively coupled equatorial waves. *Rev. Geophys.*, *47*(2). doi:
428 <https://doi.org/10.1029/2008RG000266>
- 429 Kim, J.-E., & Alexander, M. J. (2015). Direct impacts of waves on tropical cold
430 point tropopause temperature. *Geophys. Res. Lett.*, *42*(5), 1584-1592. doi: 10
431 [.1002/2014GL062737](https://doi.org/10.1002/2014GL062737)
- 432 Kim, J.-E., Alexander, M. J., Bui, T. P., Dean-Day, J. M., Lawson, R. P., Woods,
433 S., ... Jensen, E. J. (2016). Ubiquitous influence of waves on tropi-
434 cal high cirrus clouds. *Geophys. Res. Lett.*, *43*(11), 5895-5901. doi:
435 <https://doi.org/10.1002/2016GL069293>
- 436 Krämer, M., Schiller, C., Afchine, A., Bauer, R., Gensch, I., Mangold, A., ...
437 Spichtinger, P. (2009). Ice supersaturations and cirrus cloud crystal num-
438 bers. *Atmos. Chem. Phys.*, *9*(11), 3505-3522. doi: 10.5194/acp-9-3505-2009

- 439 Lim, Y., Son, S.-W., Marshall, A. G., Hendon, H. H., & Seo, K.-H. (2019). In-
 440 fluence of the QBO on MJO prediction skill in the subseasonal-to-seasonal
 441 prediction models. *Climate Dynamics*, *53*(3), 1681–1695. doi: 10.1007/
 442 s00382-019-04719-y
- 443 Marshall, A., Hendon, H., Son, S.-W., & Lim, Y. (2017, 08). Impact of the quasi-
 444 biennial oscillation on predictability of the Madden–Julian oscillation. *Clim.*
 445 *Dyn.*, *49*. doi: 10.1007/s00382-016-3392-0
- 446 Pahlavan, H. A., Fu, Q., Wallace, J. M., & Kiladis, G. N. (2021). Revisiting the
 447 Quasi-Biennial Oscillation as Seen in ERA5. Part I: Description and Momen-
 448 tum Budget. *J. Atmos. Sci.*, *78*(3), 673 - 691. doi: 10.1175/JAS-D-20-0248.1
- 449 Podglajen, A., Bui, T. P., Dean-Day, J. M., Pfister, L., Jensen, E. J., Alexander,
 450 M. J., ... Randel, W. J. (2017). Small-Scale Wind Fluctuations in the Trop-
 451 ical Tropopause Layer from Aircraft Measurements: Occurrence, Nature,
 452 and Impact on Vertical Mixing. *J. Atmos. Sci.*, *74*(11), 3847 - 3869. doi:
 453 10.1175/JAS-D-17-0010.1
- 454 Podglajen, A., Hertzog, A., Plougonven, R., & Žagar, N. (2014). Assessment of the
 455 accuracy of (re)analyses in the equatorial lower stratosphere. *J. Geophys. Res.*
 456 *Atmos.*, *119*(19), 11,166-11,188. doi: <https://doi.org/10.1002/2014JD021849>
- 457 Podglajen, A., Plougonven, R., Hertzog, A., & Jensen, E. (2018). Impact of
 458 gravity waves on the motion and distribution of atmospheric ice parti-
 459 cles. *Atmospheric Chemistry and Physics*, *18*(14), 10799–10823. doi:
 460 10.5194/acp-18-10799-2018
- 461 Richter, J. H., Butchart, N., Kawatani, Y., Bushell, A. C., Holt, L., Serva, F., ...
 462 Yukimoto, S. (2020). Response of the Quasi-Biennial Oscillation to a warm-
 463 ing climate in global climate models. *Quart. J. Roy. Meteor. Soc.*, 1-29. doi:
 464 10.1002/qj.3749
- 465 Sato, K., & Dunkerton, T. J. (1997). Estimates of momentum flux associated
 466 with equatorial kelvin and gravity waves. *J. Geophys. Res. Atmos.*, *102*(D22),
 467 26247–26261. doi: 10.1029/96JD02514
- 468 Scaife, A. A., Athanassiadou, M., Andrews, M., Arribas, A., Baldwin, M., Dunstone,
 469 N., ... Williams, A. (2014). Predictability of the quasi-biennial oscillation and
 470 its northern winter teleconnection on seasonal to decadal timescales. *Geophys.*
 471 *Res. Lett.*, *41*(5), 1752-1758. doi: 10.1002/2013GL059160
- 472 Schoeberl, M. R., Jensen, E. J., & Woods, S. (2015). Gravity waves amplify up-
 473 per tropospheric dehydration by clouds. *Earth Space Sci.*, *2*(12), 485-500. doi:
 474 <https://doi.org/10.1002/2015EA000127>
- 475 Schreiner, W., Weiss, J., Anthes, R., Braun, J., Chu, V., Fong, J., ... Zeng, Z.
 476 (2020). COSMIC-2 Radio Occultation Constellation: First Results. *Geo-*
 477 *phys. Res. Lett.*, *47*(4), e2019GL086841. doi: [https://doi.org/10.1029/](https://doi.org/10.1029/2019GL086841)
 478 [2019GL086841](https://doi.org/10.1029/2019GL086841)
- 479 Smith, D. M., Scaife, A. A., Eade, R., & Knight, J. R. (2016). Seasonal to
 480 decadal prediction of the winter north atlantic oscillation: emerging capa-
 481 bility and future prospects. *Q.J.R. Meteorol. Soc.*, *142*(695), 611-617. doi:
 482 <https://doi.org/10.1002/qj.2479>
- 483 Solomon, S., Rosenlof, K., Portmann, R., Daniel, J., Davis, S., Sanford, T., &
 484 Plattner, G.-K. (2010, 03). Contributions of Stratospheric Water Vapor to
 485 Decadal Changes in the Rate of Global Warming. *Science*, *327*, 1219-23. doi:
 486 10.1126/science.1182488
- 487 Stockwell, R. G., Mansinha, L., & Lowe, R. P. (1996). Localization of the complex
 488 spectrum: the S transform. *IEEE Transactions on Signal Processing*, *44*(4),
 489 998-1001. doi: 10.1109/78.492555
- 490 Thomas, A., Borrmann, S., Kiemle, C., Cairo, F., Volk, M., Beuermann, J., ... Ste-
 491 fanutti, L. (2002). In situ measurements of background aerosol and subvisible
 492 cirrus in the tropical tropopause region. *J. Geophys. Res. Atmos.*, *107*(D24),
 493 AAC 8-1-AAC 8-14. doi: <https://doi.org/10.1029/2001JD001385>

- 494 Vincent, R. A., & Alexander, M. J. (2020). Balloon-Borne Observations of Short
495 Vertical Wavelength Gravity Waves and Interaction With QBO Winds. *J.*
496 *Geophys. Res. Atmos.*, *125*(15), e2020JD032779. doi: 10.1029/2020JD032779
497 Yoo, C., & Son, S.-W. (2016). Modulation of the boreal wintertime Madden-Julian
498 oscillation by the stratospheric quasi-biennial oscillation. *Geophys. Res. Lett.*,
499 *43*(3), 1392-1398. doi: 10.1002/2016GL067762